Supplement of Biogeosciences, 23, 5255–5279, 2026
https://doi.org/10.5194/bg-23-5255-2026-supplement

Biogeosciences Open Access EGU

Supplement of

Biogeochemical controls on carbonate dynamics driven by methane and freshwater inputs in shallow sediments of a brackish continental shelf sea

Katarzyna Łukawska-Matuszewska et al.

Correspondence to: Katarzyna Łukawska-Matuszewska (katarzyna.lukawska-matuszewska@ug.edu.pl)

Supplementary material

S1 Diagenetic processes and their effects on the carbonate system in seawater

Table S1. Diagenetic processes and their effects on dissolved inorganic carbon (DIC) and total alkalinity (TA) based on Jørgensen (2000), Krumins et al. (2013), Raiswell and Canfield (2012), Rassmann et al. (2016), Ritger et al. (1987), and Sturm et al. (2019).

	Process	Reaction	ΔDIC	ΔAT
R1	Aerobic mineralization	$CH_2O + O_2 \rightarrow HCO_3^- + H^+$	+1	0
R2	Denitrification	$CH_2O + 0.8NO_3^- + 0.8H^+ \rightarrow CO_2 + 0.4N_2 + 1.4H_2O$	+1	+0.8
R3	Mn reduction	$CH_2O + 2MnO_2 + 3H^+ \rightarrow HCO_3^- + 2Mn^{2+} + 2H_2O$	+1	+4
R4	Fe reduction	$CH_2O + 4Fe(OH)_3 + 7H^+ \rightarrow HCO_3^- + 4Fe^{2+} + 11H_2O$	+1	+8
R5	Sulfate reduction	$CH_2O + 1/2SO_4^{2-} \rightarrow HCO_3^- + 1/2HS^- + 1/2H^+$	+1	+1
R6	Methanogenesis	$CH_2O \rightarrow 1/2CH_4 + 1/2CO_2$	+0.5	0
R7	Nitrification	$NH_4^+ + 2O_2 \rightarrow NO_3^- + H_2O + 2H^+$	0	–2
R8	Fe oxidation	$4Fe^{2+} + O_2 + 10H_2O \rightarrow 4Fe(OH)_3 + 8H^+$	0	–8
R9	Mn oxidation	$2Mn^{2+} + O_2 + 4HCO_3^- \rightarrow 2MnO_2 + 4CO_2 + 2H_2O$	0	–4
R10	H_2S oxidation	$HS^- + 2O_2 \rightarrow SO_4^{2-} + H^+$	0	–2
R11	FeS_2 oxidation	$FeS_2 + 7/2O_2 + H_2O \rightarrow Fe^{2+} + 2SO_4^{2-} + 2H^+$	0	–2
R12	Anaerobic CH_4 oxidation with Mn(IV)	$CH_4 + 4MnO_2 + 7H^+ \rightarrow HCO_3^- + 4Mn^{2+} + 5H_2O$	+1	+8
R13	Anaerobic CH_4 oxidation with Fe(III)	$CH_4 + 8Fe(OH)_3 + 15H^+ \rightarrow HCO_3^- + 8Fe^{2+} + 21H_2O$	+1	+16
R14	Anaerobic CH_4 oxidation with SO_4^{2-}	$CH_4 + SO_4^{2-} \rightarrow HS^- + HCO_3^- + H_2O$	+1	+2
R15	FeS_2 precipitation	$8Fe(OH)_3 + 15\,HS^- + SO_4^{2-} + 17H^+ \rightarrow 8FeS_2 + 28H_2O$	0	+2
R16	$CaCO_3$ precipitation	$2HCO_3^- + Ca^{2+} \rightarrow CaCO_3 + H_2O + CO_2$	–1	–2
R17	$CaCO_3$ dissolution	$CaCO_3 + H_2O + CO_2 \rightarrow Ca^{2+} + 2HCO_3^-$	+1	+2

S2 Sampling stations

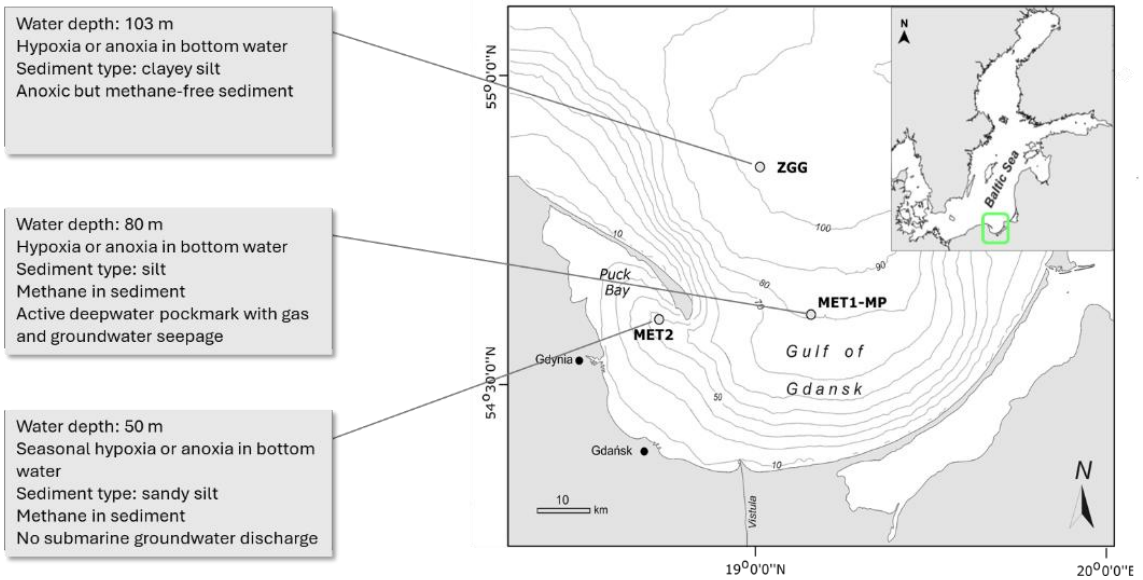

Figure S1: Map of the study area showing the location of research stations MET1-MP, MET2, and ZGG. Sediment types at each station follow Brodecka et al. (2013).

S3 Sediment porosity, water content and loss on ignition, redox conditions, and pore-water pH

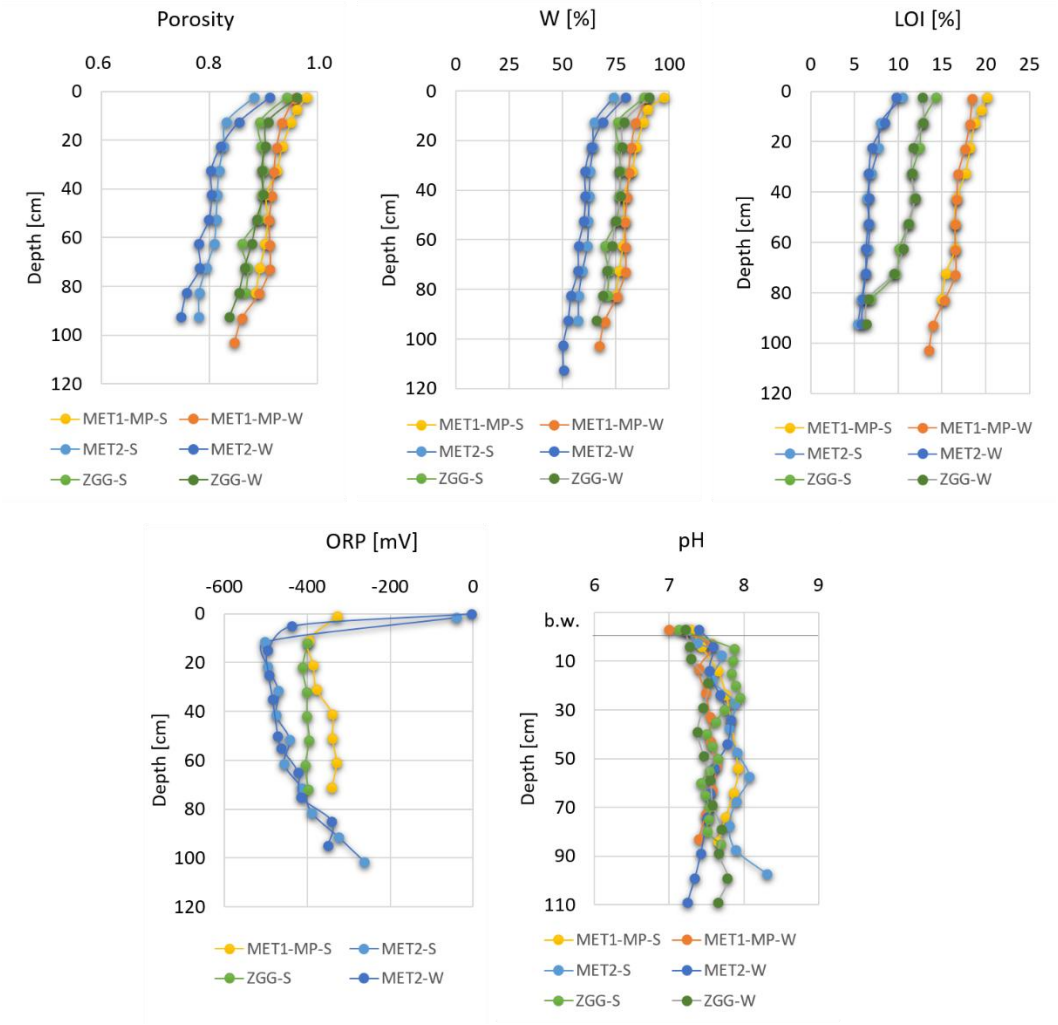

Figure S2: Vertical profiles of porosity, water content (W), loss on ignition (LOI), oxidation–reduction potential (ORP), and pore-water pH at stations MET1-MP, MET2, and ZGG. ORP in two seasons was measured only at MET2, at MET1-MP and ZGG ORP was measured only in July 2023 (b.w. – bottom water).

S4 Stable isotopes of carbon and hydrogen in gases

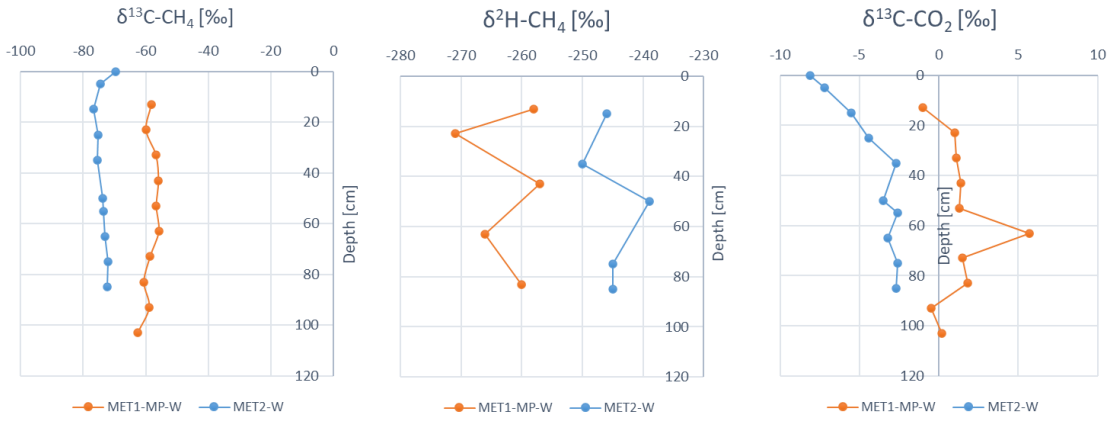

Figure S3: Depth profiles of δ^{13}C-CH_4, δ^{13}C-CO_2, and δ^{2}H-CH_4 in gases from stations MET1-MP and MET2 (winter 2024).

S5 Dissolved inorganic carbon production versus sulfate consumption

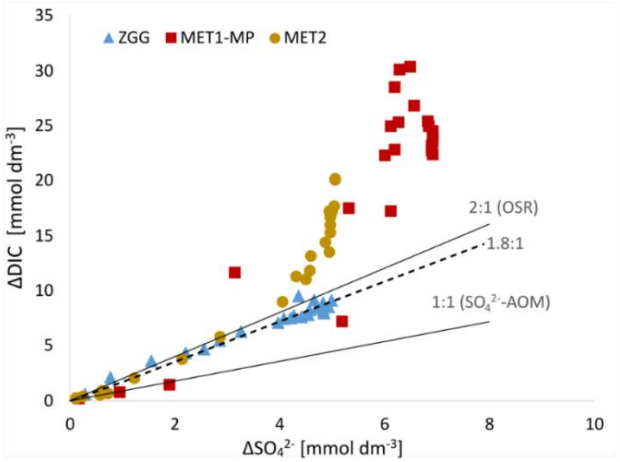

Figure S4: Relationship between dissolved inorganic carbon production (ΔDIC) and sulfate consumption (ΔSO_4^{2-}) in pore waters from stations ZGG, MET1-MP, and MET2. Values were corrected for molecular diffusion using the approach of Berner (1980). Sulfate consumption and DIC production were calculated as the difference between pore-water and bottom-water concentrations within each sediment layer. Diagonal lines indicate theoretical $\Delta DIC/\Delta SO_4^{2-}$ ratios for organoclastic sulfate reduction (OSR) and sulfate-driven anaerobic oxidation of methane (SO_4^{2-}–AOM). At station ZGG, pore-water ratios are consistent with OSR (mean $\Delta DIC/\Delta SO_4^{2-} = 1.85$). At stations MET1-MP and MET2, ratios indicative of OSR, SO_4^{2-}–AOM, or mixed processes occur only in surface sediments (0–13 cm at MET1-MP; 0–20 cm at MET2).

S6 Determination of rates of organoclastic sulfate reduction (OSR) and anaerobic oxidation of methane (AOM)

Table S2. Kinetic parameters and potential rate of sulfate reduction.

Sample	Test 1*	Test 2*	Average rate*	Kinetic parameters	
	[µmol dm^{-3} d^{-1}]			K_M	V_{max} [µmol dm^{-3} d^{-1}]
MET1_MP_1	116.4	211.5	163.9	0.07	250
MET1_MP_2	21.2	24.2	22.7	0.01	22
MET1_MP_3	18.3	11.8	15.1	0.005	18
MET1_MP_4	16.4	16.2	16.3	0.004	17
MET1_MP_5	17.4	18.6	18.0	0.004	18
MET2_1	20.7	20.7	20.7	0.004	28
MET2_2	51.2	51.2	48.1	0.01	54
MET2_3	33.3	39.5	36.4	0.005	36
MET2_4	34.8	26.6	30.7	0.005	34
MET2_5	41.2	42.4	41.8	0.005	46
ZGG_1	24.8	23.3	24.3	0.003	26
ZGG_2	45.4	46.6	46.0	0.02	51
ZGG_3	25.2	25.5	25.4	0.004	26
ZGG_4	33.3	34.2	33.8	0.004	32
ZGG_5	33.6	33.0	33.3	0.004	32

* Potential rate at concentration of substrate 0.1 M sulfate

Table S3. Parameters and analytical conditions for the determination of CO_2 concentration resulting from anaerobic oxidation of methane.

Sample	Analytical conditions						Standard [CO_2]	
	vol. [cm^3]	^{13}C-CH_4 [10^{-3} cm^3]	headspace [cm^3]	incubation [h]	peak area [CO_2]	activity [mmol dm^{-3} d^{-1}]	conc. [%]	peak area [CO_2]
MET1_MP_1	2	100	18	70	558	0.095	0.2	1634 ±9.90 (Std.Dev.)
MET1_MP_2	2	100	18	70	622	0.106		
MET1_MP_3	2	100	18	70	6349	1.077		
MET1_MP_4	2	100	18	70	346	0.059		
MET1_MP_5	2	100	18	70	4310	0.731		
MET2_1	2	100	18	76	212	0.033		
MET2_2	2	100	18	76	36	0.006		
MET2_3	2	100	18	76	47	0.007		
MET2_4	2	100	18	76	56	0.009		
MET2_5	2	100	18	76	52	0.008		
ZGG_1	2	100	18	71	59	0.010		
ZGG_2	2	100	18	71	54	0.009		
ZGG_3	2	100	18	71	61	0.010		
ZGG_4	2	100	18	71	55	0.009		
ZGG_5	2	100	18	71	45	0.008		

S7 Bulk mineralogy

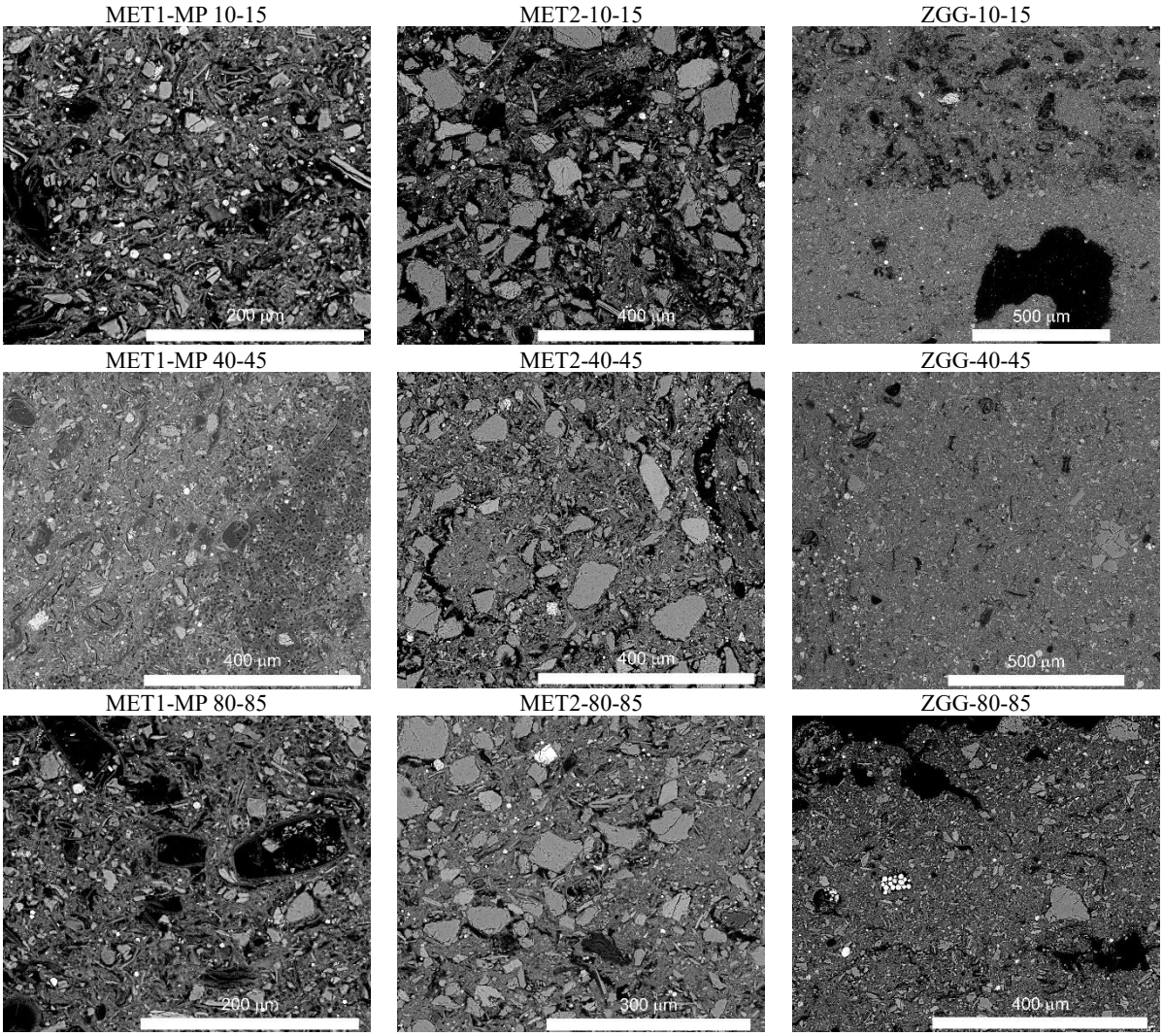

Figure S5: SEM-BSE images of sediment thin sections. Gray grains represent detrital components. Bright spots correspond to pyrite framboids. Dark gray areas indicate clay–silica–organic aggregates. Black areas represent pores.

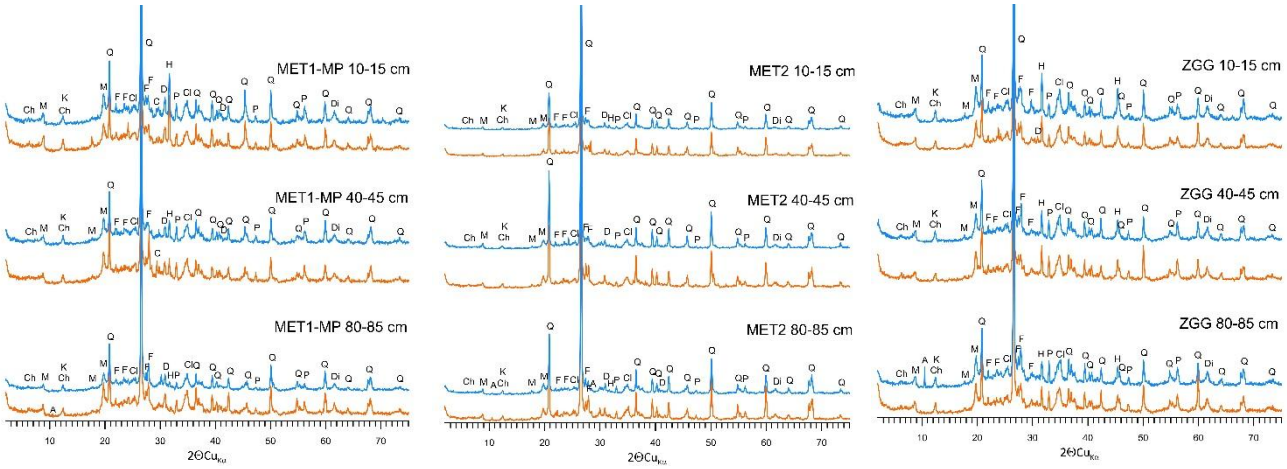

Figure S6: Mineral composition of sediments from stations MET1-MP, MET2, and ZGG (blue – winter, orange – summer) determined by powder X-ray diffraction (PXRD). Abbreviations: Q = quartz; H = halite; F = feldspar; M = mica/illite; K = kaolinite; Ch = chlorite; P = pyrite; D = dolomite; C = calcite; Cl = clay minerals; Di = dioctahedral phyllosilicates. Halite is an artifact precipitated from pore water upon freeze-drying.

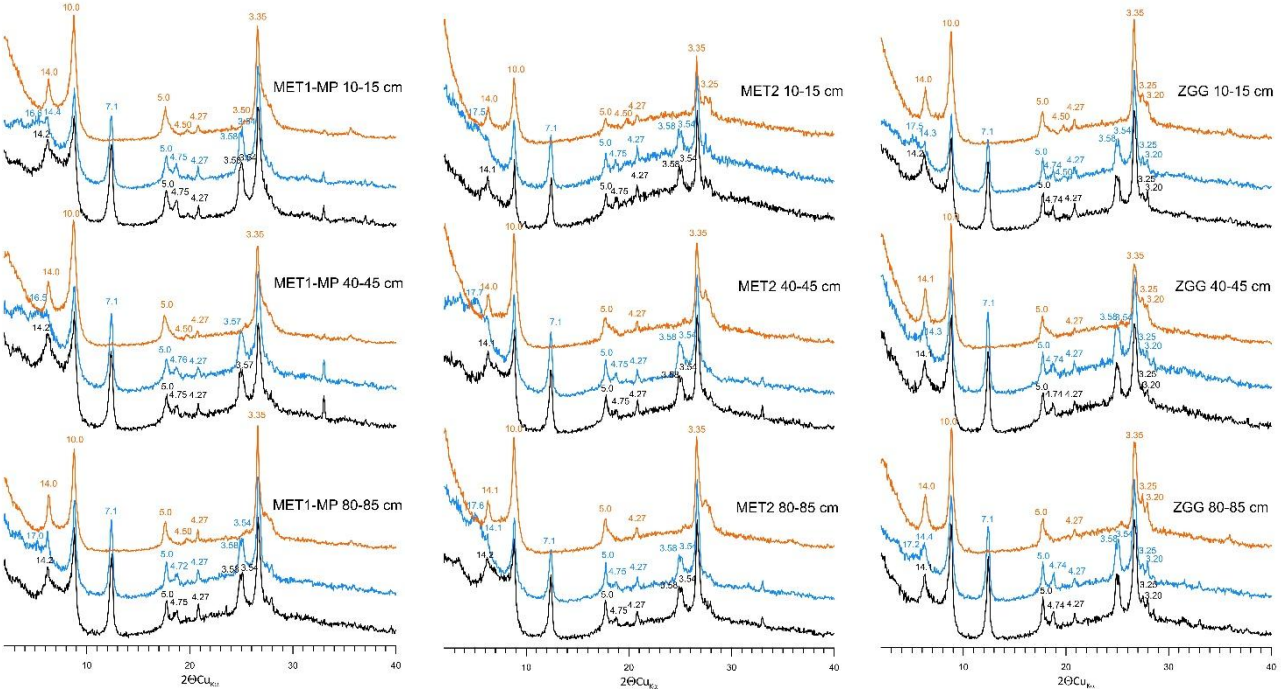

Figure S7: PXRD patterns of the clay fraction. Black patterns represent air-dried samples. Blue patterns represent ethylene glycol–saturated samples. Orange patterns represent samples heated to 500°C. d-spacings (Å) are indicated above peaks. Broad features at low 2θ (>20 Å) reflect instrumental artifacts.

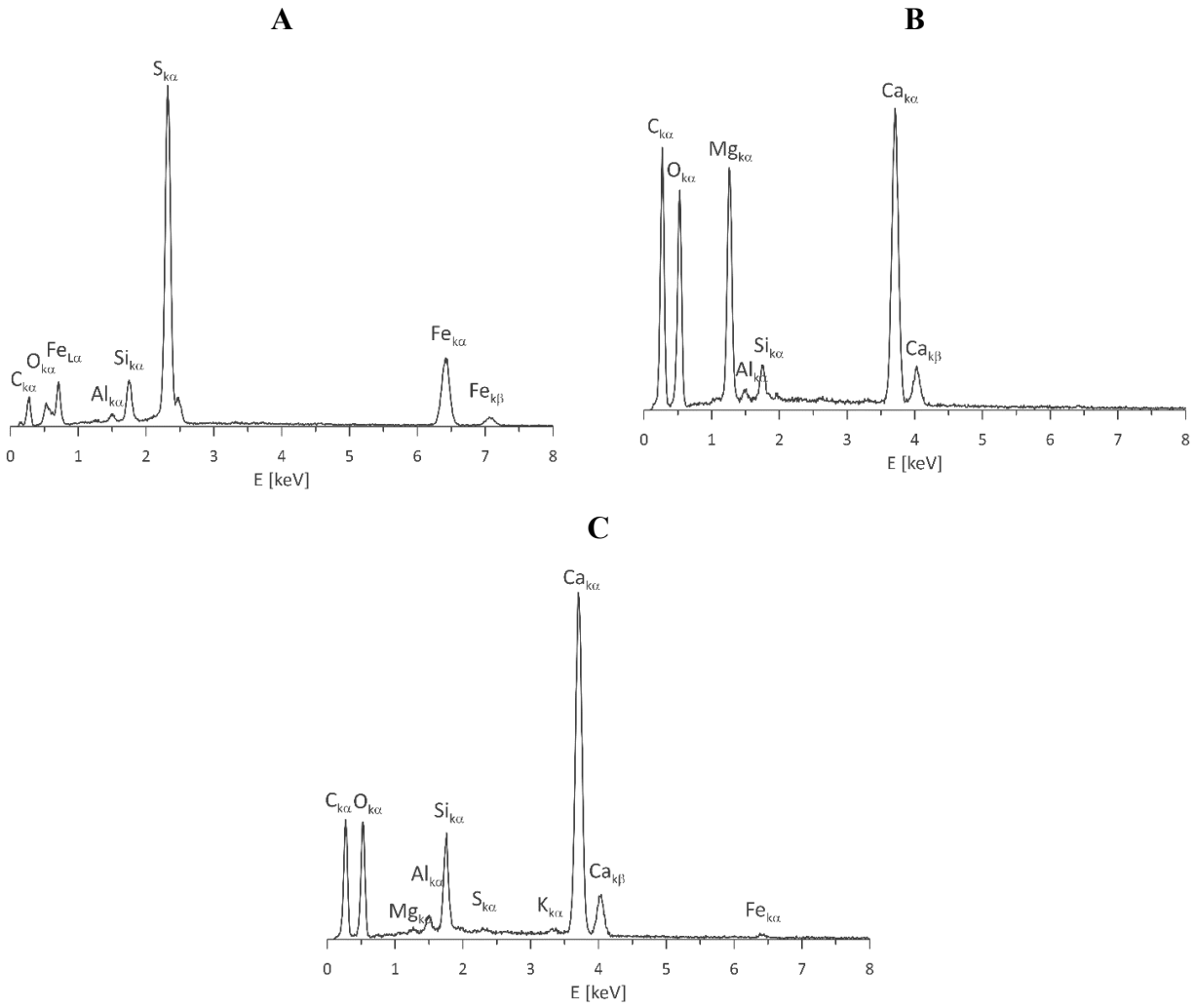

Figure S8: Representative EDS spectra of A: pyrite (MET1_MP 40–45 cm), B: dolomite (MET1_MP 10–15 cm), and C: calcite (ZGG 40–45 cm)).

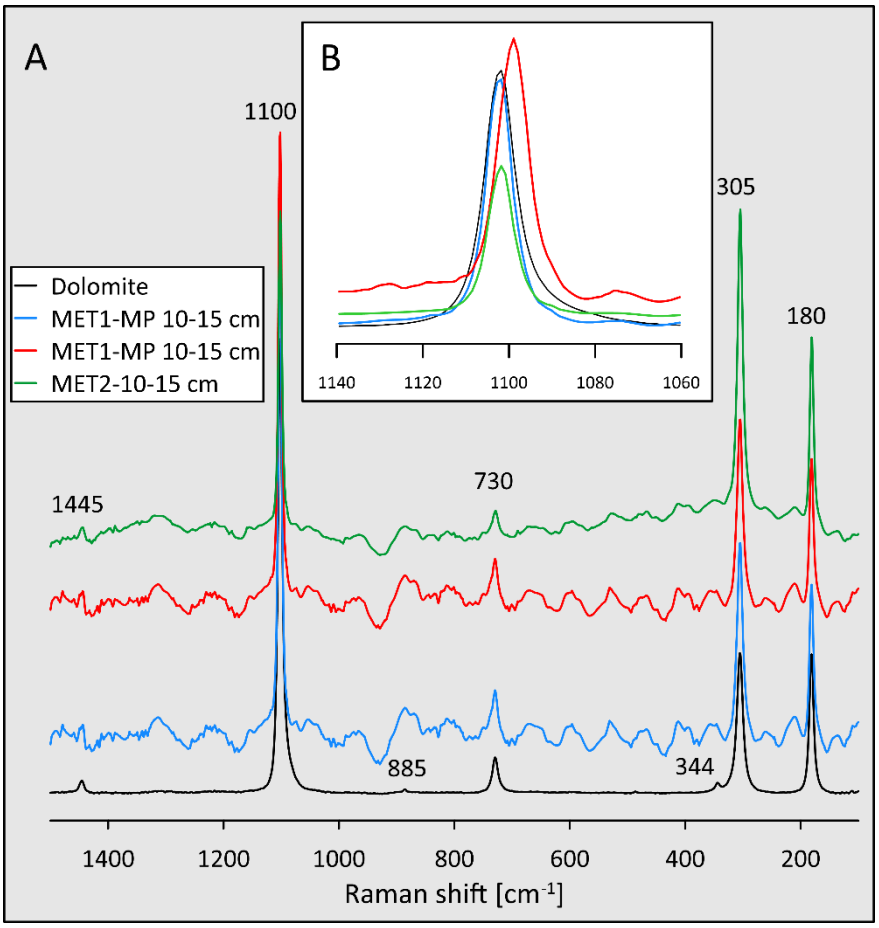

Figure S9: A: Raman spectra of representative Ca-Mg carbonate crystals from MET1-MP (blue and red) and MET2 stations (green) compared to the spectrum of dolomite from Rędziny quarry (black). B: Comparison of the intensity and position of the symmetric stretching band at ca. 1100 cm^{-1} (the intensity scale is identical for all the spectra).

S8 Mössbauer spectroscopy

Table S4. ^{57}Fe Mössbauer parameters. A = relative spectral area, reflecting the proportion of Fe in each phase; IS = isomer shift relative to α-Fe; QS = quadrupole splitting; Γ = line width. S = summer; W = winter. * - parameters typical also for Fe in siderite.

sample	iron form	A (%)		IS (mm/s)		QS (mm/s)		Γ (mm/s)	
		S	W	S	W	S	W	S	W
MET1-MP 10-15	Fe^{2+}(pyrite)	59	60	0.30	0.30	0.61	0.61	0.33	0.32
	Fe^{2+}(silicate-1)	23	22	1.12	1.12	2.69	2.67	0.33	0.32
	Fe^{2+} (silicate-2)*	6	5	1.20	1.20	1.92	1.92	0.36	0.36
	Fe^{3+}	12	13	0.48	0.49	0.83	0.81	0.54	0.55
MET1-MP 40-45	Fe^{2+}(pyrite)	58	57	0.30	0.30	0.60	0.61	0.32	0.33
	Fe^{2+}(silicate-1)	24	20	1.12	1.12	2.67	2.68	0.34	0.32
	Fe^{2+} (silicate-2)*	4	7	1.19	1.22	1.87	2.00	0.27	0.37
	Fe^{3+}	14	16	0.49	0.47	0.76	0.86	0.54	0.73
MET1-MP 80-85	Fe^{2+}(pyrite)	53	50	0.30	0.30	0.61	0.62	0.35	0.36
	Fe^{2+}(silicate-1)	26	22	1.12	1.11	2.66	2.67	0.35	0.32
	Fe^{2+} (silicate-2)*	4	6	1.15	1.16	1.83	1.97	0.34	0.39
	Fe^{3+}	17	22	0.47	0.46	0.79	0.76	0.54	0.52
MET2 10-15	Fe^{2+}(pyrite)	53	54	0.30	0.30	0.61	0.61	0.35	0.33
	Fe^{2+}(silicate-1)	17	20	1.12	1.10	2.71	2.67	0.32	0.32
	Fe^{2+} (silicate-2)*	7	4	1.22	1.19	1.92	1.90	0.42	0.30
	Fe^{3+}	24	22	0.40	0.44	0.83	0.78	0.58	0.57
MET2 40-45	Fe^{2+}(pyrite)	54	55	0.30	0.30	0.61	0.62	0.37	0.37
	Fe^{2+}(silicate-1)	19	21	1.12	1.11	2.71	2.68	0.33	0.33
	Fe^{2+} (silicate-2)*	5	5	1.21	1.18	1.98	1.96	0.34	0.38
	Fe^{3+}	22	19	0.42	0.47	0.80	0.76	0.59	0.52
MET2 80-85	Fe^{2+}(pyrite)	60	59	0.30	0.30	0.61	0.60	0.33	0.31
	Fe^{2+}(silicate-1)	20	17	1.12	1.12	2.69	2.69	0.34	0.30
	Fe^{2+} (silicate-2)*	4	6	1.18	1.23	1.87	1.96	0.36	0.35
	Fe^{3+}	16	18	0.47	0.40	0.79	0.86	0.58	0.56
ZGG 10-15	Fe^{2+}(pyrite)	56	58	0.30	0.31	0.60	0.59	0.34	0.33
	Fe^{2+}(silicate-1)	28	22	1.12	1.12	2.68	2.67	0.32	0.31
	Fe^{2+} (silicate-2)*	5	6	1.20	1.22	2.00	2.00	0.39	0.37
	Fe^{3+}	11	14	0.52	0.40	0.76	0.94	0.46	0.49
ZGG 40-45	Fe^{2+}(pyrite)	61	55	0.30	0.30	0.61	0.60	0.33	0.30
	Fe^{2+}(silicate-1)	18	24	1.13	1.12	2.70	2.66	0.29	0.30
	Fe^{2+} (silicate-2)*	11	6	1.22	1.22	2.18	2.03	0.47	0.36
	Fe^{3+}	10	15	0.42	0.43	0.93	0.82	0.55	0.53
ZGG 80-85	Fe^{2+}(pyrite)	53	56	0.30	0.30	0.61	0.60	0.34	0.31
	Fe^{2+}(silicate-1)	21	25	1.13	1.12	2.69	2.66	0.30	0.32
	Fe^{2+} (silicate-2)*	12	7	1.18	1.23	2.26	2.03	0.46	0.40
	Fe^{3+}	14	12	0.46	0.45	0.76	0.88	0.65	0.50

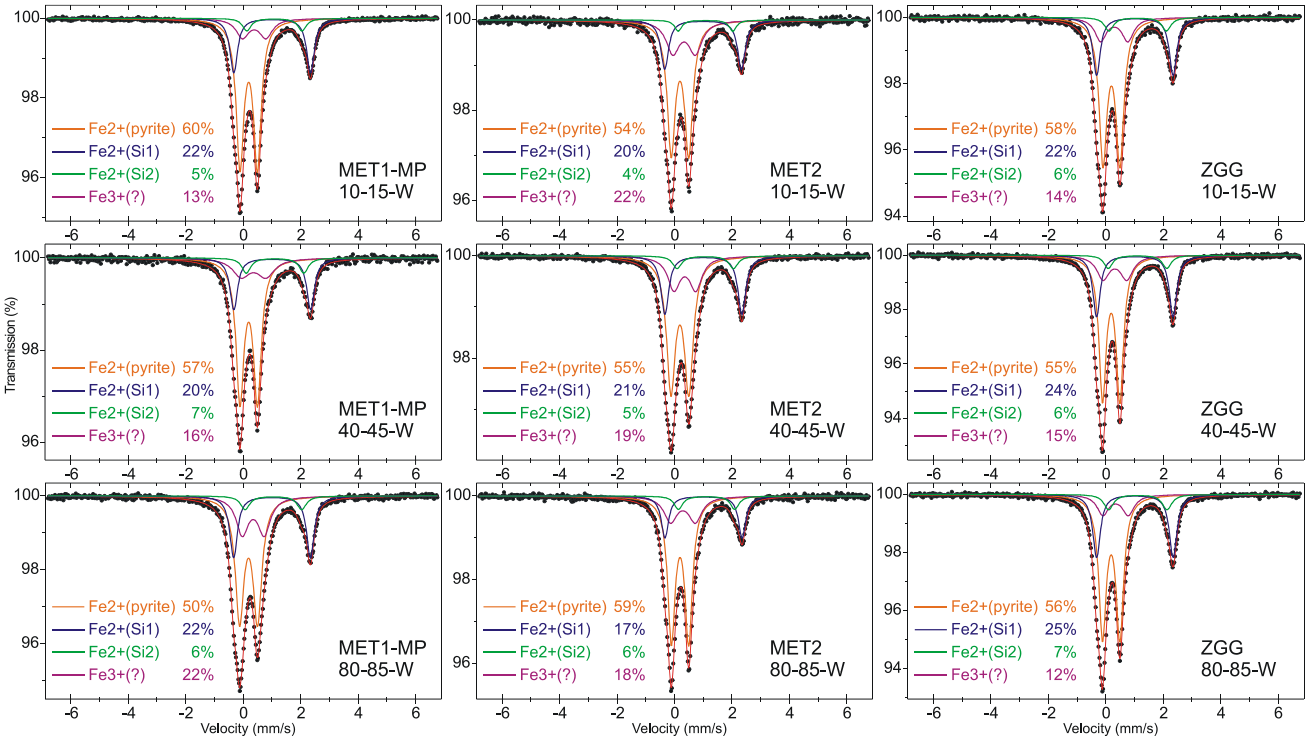

Figure S10: ^{57}Fe Mössbauer spectra of sediments collected in winter.

S9 Saturation indices from geochemical modelling

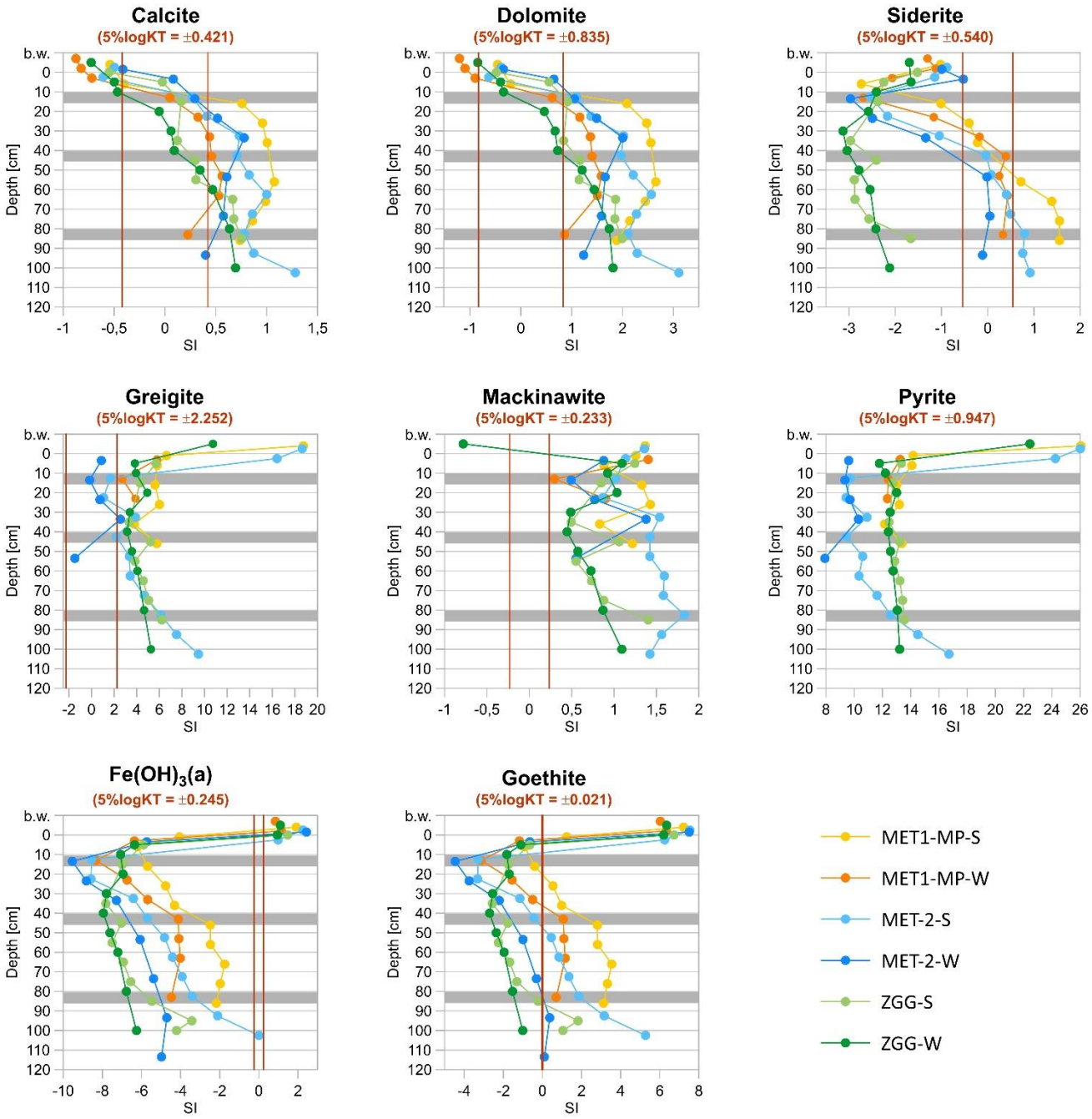

Figure S11: Saturation indices for selected minerals at stations MET1-MP, MET2, and ZGG in July 2023 (S) and February 2024 (W), calculated using PHREEQC. Sediment depths used for mineralogical analyses are indicated by gray bars.

References

Berner, R.A.: Early Diagenesis: A Theoretical Approach. Princeton University Press; 241 pp., 1980.

Jørgensen, B.B.: Bacteria and Marine Biogeochemistry. In: Schulz, H.D., Zabel, M. (eds) Marine Geochemistry. Springer, Berlin, Heidelberg. https://doi.org/10.1007/978-3-662-04242-7_5, 2000.

Krumins, V., Gehlen, M., Arndt, S., Van Cappellen, P., and Regnier, P.: Dissolved inorganic carbon and alkalinity fluxes from coastal marine sediments: model estimates for different shelf environments and sensitivity to global change, Biogeosciences, 10, 371–398, https://doi.org/10.5194/bg-10-371-2013, 2013.

Raiswell, R., Canfield, D.E.: The iron biogeochemical cycle past and present. Geochemical perspectives, 1(1), 1-220, 2012.

Rassmann, J., Lansard, B., Pozzato, L., and Rabouille, C.: Carbonate chemistry in sediment porewaters of the Rhône River delta driven by early diagenesis (northwestern Mediterranean), Biogeosciences, 13, 5379–5394, https://doi.org/10.5194/bg-13-5379-2016, 2016.

Ritger, S., Carson, B., Suess, E.: Methane-derived Authigenic Carbonates Formed by Subduction-induced Pore-water Expulsion along the Oregon/Washington Margin. Geological Society of America Bulletin - GEOL SOC AMER BULL. 98. 10.1130/0016-7606(1987)98<147:MACFBS>2.0.CO;2., 1987.

Sturm A., Fowle D.A., Jones C., et al.: Rates and pathways of CH_4 oxidation in ferruginous Lake Matano, Indonesia. Geobiology. 17:294–307. https://doi.org/10.1111/gbi.12325, 2019.